Geochemistry, Geophysics, Geosystems

RESEARCH ARTICLE
10.1029/2019GC008766

Key Points:
- Mantle anisotropy above and beneath the slab and crustal anisotropy in the overriding plate are investigated
- Subslab entrained flow deflected by the mantle transition zone accounts for the change of anisotropy from trench-normal to parallel
- Pattern of mantle wedge anisotropy reflects trench-parallel flow escaped from subslab and modulated by a slab window

Supporting Information:
- Supporting Information S1
- Table S1
- Table S2
- Table S3
- Table S4

Correspondence to:
F. Kong, and J. Li,
kongfs@sio.org.cn;
jbli@sio.org.cn

Citation:
Kong, F., Gao, S. S., Liu, K. H., Zhang, J., & Li, J. (2020). Seismic anisotropy and mantle flow in the Sumatra subduction zone constrained by shear wave splitting and receiver function analyses. *Geochemistry, Geophysics, Geosystems*, *21*, e2019GC008766. https://doi.org/10.1029/2019GC008766

Received 17 OCT 2019
Accepted 28 JAN 2020
Accepted article online 30 JAN 2020

Seismic Anisotropy and Mantle Flow in the Sumatra Subduction Zone Constrained by Shear Wave Splitting and Receiver Function Analyses

Fansheng Kong[1,2], Stephen S. Gao[2], Kelly H. Liu[2], Jie Zhang[1], and Jiabiao Li[1]

[1]Key Laboratory of Submarine Geosciences, Second Institute of Oceanography, Ministry of Natural Resources, Hangzhou, China, [2]Geology and Geophysics Program, Missouri University of Science and Technology, Rolla, MO, USA

Abstract To systematically investigate seismic azimuthal anisotropy in the Sumatra subduction zone and probe mantle dynamics associated with the subduction of the Australian Plate beneath the Sunda Plate, a total of 169 pairs of teleseismic XKS (including PKS, SKKS, SKS) and 115 pairs of local *S* splitting parameters are obtained using broadband seismic data recorded at ~70 stations. Additionally, crustal anisotropy in the overriding Sunda Plate is measured by analyzing the moveout of *P*-to-*S* conversions from the Moho using a sinusoidal function. Comparison between the three sets of anisotropy measurements obtained using shear waves with different depths of origin suggests that (1) the crust of the Sunda Plate is anisotropic with mostly trench-parallel fast orientations and a mean splitting time of 0.28 ± 0.05 s; (2) the mantle wedge is azimuthally anisotropic with dominantly trench-parallel fast orientations and splitting times ranging from 0.22 to 0.81 s, which generally increase with the focal depth; and (3) subslab anisotropy is mostly trench-normal beneath the fore-arc region with an averaged splitting time of 1.48 ± 0.06 s, and becomes trench-parallel beneath the arc and back-arc areas with a mean splitting time of 0.33 ± 0.04 s. The resulting lateral and vertical distributions of anisotropy obtained using splitting of three types of shear waves advocate the presence of an entrained subslab flow that is deflected by the mantle transition zone. The flow enters the mantle wedge through a slab window and flows horizontally parallel to the trench.

1. Introduction

The Sumatra subduction zone (Figure 1) represents the subduction of the Australian Plate beneath the Sunda Plate along the Sumatran Trench, with a subduction rate of ~64 mm/year at a direction of 40° clockwise from north in a fixed hot spot frame (Argus et al., 2011). The oblique subduction is responsible for the numerous devastating earthquakes including the 26 December 2004 M_w 9.1–9.3 megaearthquake (Stein & Okal, 2005), and is home to some of the most active volcanoes in the world including the Toba supervolcano which created the largest terrestrial Quaternary caldera in the world (Chesner et al., 1991). The Toba supervolcano is believed to have significantly affected the biosphere of the whole Earth during its last eruption at ~74,000 years ago (e.g., Chesner & Luhr, 2010), when 2,800–5,300 km^3 of material was ejected (Chesner et al., 1991). The origin of the ejected materials remains enigmatic in terms of whether the thermal supply was mainly caused by the upward migration of volatiles associated with the Investigator Fracture Zone, or was linked to subslab thermal upwelling through a slab window (e.g., Koulakov et al., 2016) that has been suggested based on seismic tomography and other studies beneath northern Sumatra (Figure 1; Hall & Spakman, 2015; S. Liu et al., 2018). The latter hypothesis implies that the subslab mantle material, once enters the mantle wedge through the slab window, may have a horizontal branch that can be detected and characterized using various techniques such as shear wave splitting.

As demonstrated by numerous previous studies, understanding the mantle flow field in a subduction system is essential for probing mantle dynamics and comprehending the relationship between surface dynamic processes and mantle deformation associated with plate subduction (e.g., K.H. Liu et al., 2008; Long & Silver, 2009; Long & Wirth, 2013; Ma et al., 2019; Tang et al., 2014; Venereau et al., 2019). The mantle flow system can be readily characterized by the orientation and strength of seismic azimuthal anisotropy (Zhang & Karato, 1995), which is quantifiable by shear wave splitting (SWS) analysis using shear waves originating from local events occurred in the *S* wave window (e.g., K.H. Liu et al., 2008), sinusoidal moveout of *P*-to-*S* converted waves from the Moho (e.g., H. Liu & Niu, 2012; Rumpker et al., 2014), and SWS analysis of teleseismic PKS, SKKS, and SKS waves (collectively called XKS hereafter; Silver & Chan, 1991).

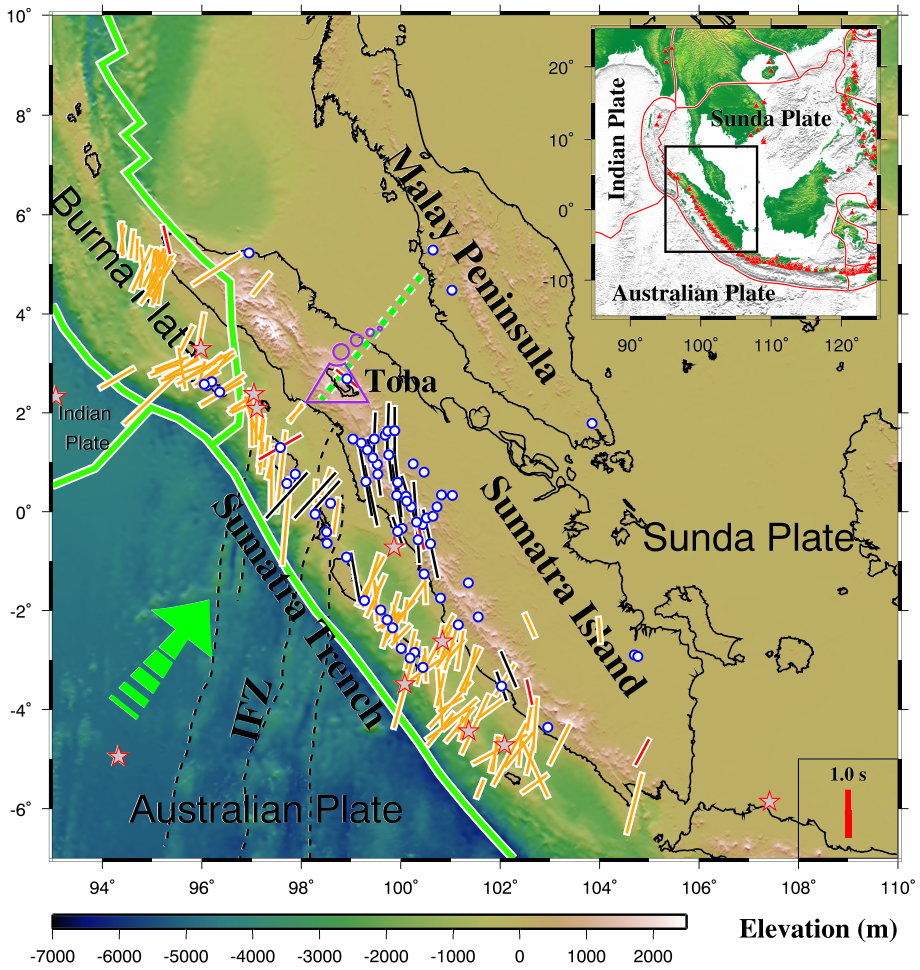

Figure 1. Topographic relief map of the study area showing the broadband seismic stations used in the study (circles) and epicenters of magnitude ≥7.5 earthquakes occurred since 2000 (stars). The bars denote the shear wave splitting parameters from studies of Collings et al. (2013) (black bars) and Hammond et al. (2010) (red bars), and the source-side shear wave splitting measurements from Lynner and Long (2014) (orange bars), with the orientation of the bars representing the fast orientation and the length being proportional to the splitting time. The green dash line marks the slab window beneath northern Sumatra (Hall & Spakman, 2015). The green arrow shows the Australian Plate motion direction relative to the Sunda Plate from the NNR-MOREVEL56 model (Argus et al., 2011). The purple volcano symbol represents the Toba Caldera. IFZ = Investigator Fracture Zone. The black rectangle in the inset map indicates the study area.

It has long been recognized that when a shear wave travels with a steep angle of incidence through an azimuthally anisotropic structure with a horizontal axis of symmetry, it splits into the fast and slow components that polarize orthogonally (Ando et al., 1980). A splitting time (δt) is accumulated along the raypath due to the difference in propagating velocities of the fast and slow waves, which can be used to constrain the strength or thickness of the layer of anisotropy (e.g., Silver & Chan, 1991). The polarization orientation of the fast shear wave (fast orientation or Φ) conveys essential information about the orientation of seismic azimuthal anisotropy (Silver & Chan, 1991). In the upper mantle, azimuthal anisotropy is generally regarded as the consequence of lattice preferred orientation (LPO) of olivine (Zhang & Karato, 1995), which is the most abundant mineral in the upper mantle (Ben Ismail & Mainprice, 1998). For *A*-, *C*-, and *E*-type olivine fabrics, which contain the dominant fabric type in subslab areas and in most part of the mantle wedge (Karato et al., 2008), the fast orientation of the resulting azimuthal anisotropy is parallel to the mantle flow direction. Under relatively high-stress and water-rich conditions such as those found along a narrow zone close to the trench in the mantle wedge above some subducting slabs, *B*-type olivine fabric could develop, for which the resulting fast orientation is perpendicular to the mantle flow direction (Jung & Karato, 2001).

To better understand subduction dynamics and probe the mantle flow fields associated with slab subduction in one of the seismically most active areas in the world, a number of shear wave splitting studies have been conducted in the vicinity of the Sumatra subduction zone (Candra et al., 2017; Collings et al., 2013; Hammond et al., 2010; Long & Silver, 2008; Lynner & Long, 2014; Walpole et al., 2017). Previous studies (Figure 1) that utilize source-side shear wave splitting analysis aiming at imaging subslab anisotropic structures led to conflicting geodynamic implications. Lynner and Long (2014), for example, attributed the resulting anisotropy measurements whose orientations are dominantly trench-orthogonal to an entrained two-dimensional subslab flow beneath the Sumatra subduction zone. In comparison, the subslab anisotropy constrained by Walpole et al. (2017) was explained by tilted transverse isotropy with a slow axis of symmetry normal to the slab plane, which is equivalent to a trench-parallel fast orientation. The differences in the observation and interpretation of the splitting results could be attributed to the influence of anisotropy along the raypath of the source-side *S* waves in the lower mantle (Walpole et al., 2017). Shear wave splitting analyses utilizing teleseismic XKS phases can avoid this possible contamination by removing all but radially polarizing energy after the *P*-to-*S* conversion at the core–mantle boundary on the receiver side, and consequently only characterize azimuthal anisotropy on the receiver side. Candra et al. (2017) and Hammond et al. (2010) attributed the SKS and SKKS splitting measurements to anisotropic structures in the subducted Australian slab and the lithosphere of the overriding Sunda Plate, and suggested that the subslab region and the mantle wedge is mostly isotropic. These conclusions are largely inconsistent with the results of Collings et al. (2013), which utilized both teleseismic and local *S* waves and suggested the existences of a subslab entrained flow and a two-dimensional corner flow in the mantle wedge. Their results also indicate that the subducted slab has limited contributions to the observed SKS splitting. The inconsistencies in the resulting anisotropy measurements and the geodynamic implications among the previous studies are probably resulted from the inadequate spatial coverage of the resulting SWS parameters and limited vertical resolution of the SWS technique caused by the near-vertical incidence angle of the XKS raypaths.

In this study, teleseismic XKS, local *S* phases, and *P*-to-*S* conversions at the Moho are utilized to systematically investigate the anisotropic structures in the crust of the overriding plate, the mantle wedge, the subducted slab, and the subslab mantle of the Sumatra subduction zone, for the purpose of characterizing the mantle flow fields associated with the subduction process above and below the subducted slab. To our knowledge, this is the first time when all the three anisotropy measuring techniques are applied to investigate anisotropy layering in this area.

2. Data

The broadband seismic data set utilized for the anisotropy investigations was recorded by 67 stations (Figure 1) covering a 26-year recording period from 1993 to 2019. Data from 61 of the 67 stations were requested from the Incorporated Research Institutions for Seismology Data Management Center, and data from the other six stations were provided by the GEOFON Data Centre of the GFZ German Research Centre for Geosciences. The data set for the XKS splitting analyses was requested by using the following two criteria: (1) the epicentral distance range is 120° to 180° for PKS, 95° to 180° for SKKS, and 83° to 180° for SKS and (2) the cutoff magnitude is 5.6 for events with a focal depth smaller than 100 km and 5.5 for deeper events (K.H. Liu & Gao, 2013).

For local *S* splitting analyses, the epicentral distance range is 0° to 7°, and the cutoff magnitude is 4.0. To avoid interference of wave-type conversions from the free surface, we only used data from events inside the *S* wave window, which is a cone-shaped region in which the events have an angle of incidence of θ or smaller, where θ is defined as $\sin^{-1}V_s/V_p$ (Evans, 1984), where the *P* and *S* wave velocity ratio, V_p/V_s, is taken as 1.732.

For measuring crustal anisotropy using the sinusoidal moveout of the *P*-to-*S* conversions from the Moho (Pms) on the receiver functions (RFs; Kong et al., 2016; H. Liu & Niu, 2012; Rumpker et al., 2014), we requested data from the data centers for events within the epicentral distance range of 30° to 180° with a cutoff magnitude M_c, which is expressed as $M_c = 5.2+(\Delta - 30.0)/(180.0 - 30.0) - D/700$, where Δ denotes the epicentral distance in degree and D represents the event depth in kilometers. This equation is intended to balance the quality and quantity of the seismic data to be requested (K.H. Liu & Gao, 2010). Figure 2 shows distribution of the events used for XKS and local *S* wave splitting and receiver function analyses.

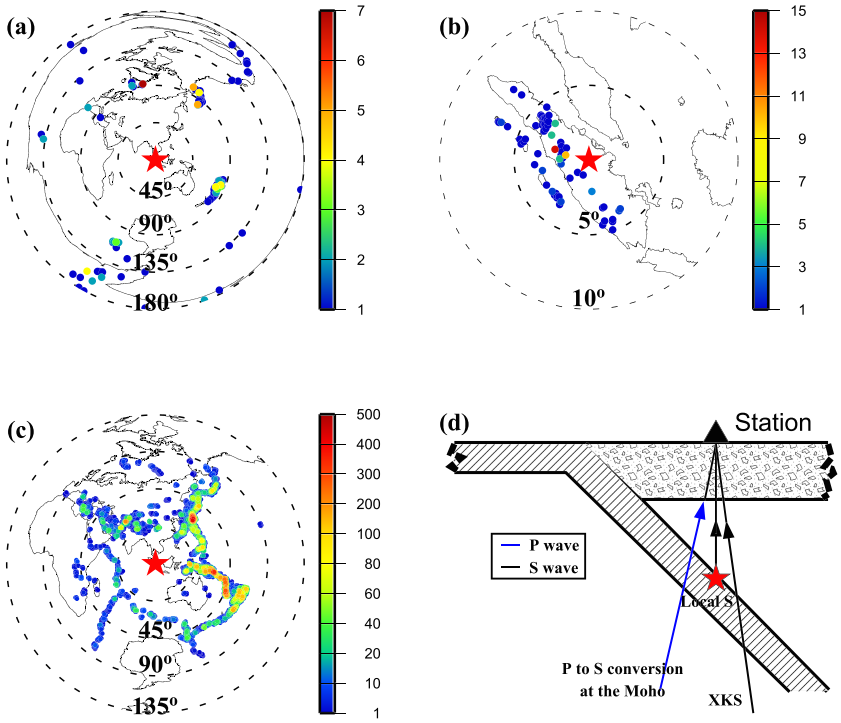

Figure 2. (a). An azimuthal equidistant projection map showing the earthquakes that resulted in at least one well-defined (Quality A or B) XKS SWS measurements. The numerals indicate the distance (in degree) from the center of the study area, and the color of the circles with a radius of 1° represents the number of measurements in the circles. (b) Same as (a) but for local *S* splitting. (c) Same as (a) but for measuring crustal anisotropy using *P*-to-*S* receiver functions. The color represents the number of receiver functions from earthquakes in the circles. (d) A schematic diagram showing the raypath of various *S* waves (black lines) involved in the study. The blue portion of the leftmost line is the direct *P* wave that generates *P*-to-*S* conversion from the Moho of the overriding plate.

3. Methods

3.1. Shear Wave Splitting Using XKS and Local *S*

For XKS splitting measurements, we used the approach described in K.H. Liu and Gao (2013), which is based on the transverse minimization method of Silver and Chan (1991). The resulting optimal pair of splitting parameters corresponds to the minimum energy on the corrected transverse component (Figure 3). For measuring splitting using local events, the optimal pair of splitting parameters for the local *S* waves corresponds to the δt and Φ that result in the minimum of the smaller of the two eigenvalues associated with the covariance matrix, which is equivalent to the most-linear particle pattern (Figure 4; Silver & Chan, 1991). The errors in the resulting SWS parameters using XKS and local *S* are estimated by applying the inverse *F* test, which represents the 95% confidence level (Silver & Chan, 1991). To enhance the signal-to-noise ratio, the XKS events were band-pass filtered with frequencies of 0.04 and 0.5 Hz, and for the local *S* events, they are 0.1 and 1 Hz. The initial time window used for measuring the XKS parameters was set as (t_a − 5 s, t_a + 20 s), while that for local *S* wave is set as (t_a − 1 s, t_a + 5 s), where t_a represents the predicted XKS or *S* arrival time calculated based on the IASP91 Earth model, and was adjusted during the manual checking stage to only include the XKS or local *S* waves. The resulting SWS measurements were then ranked to Quality A (excellent), B (good), C (unusable), and N (null) by applying an objective ranking procedure based on the signal-to-noise ratio on the original and corrected radial and transverse components, as described in K.H. Liu et al. (2008) and K.H. Liu and Gao (2013). All the SWS measurements were manually checked for ensuring reliability, in which process the time window for calculating the SWS parameters and the rank were manually adjusted if necessary. For a small portion (~5%) of measurements, the band-pass-filtering frequencies were adjusted to filter out strong noises. Figures 3 and 4 show examples of SWS measurements from the XKS and local *S* events, respectively.

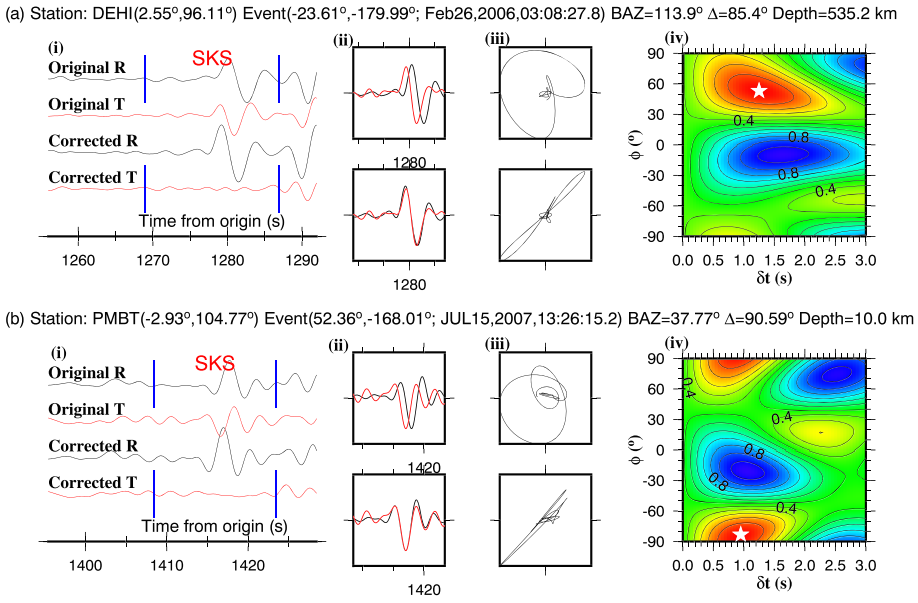

Figure 3. Examples of XKS SWS measurements from Stations (a) DEHI and (b) PMBT. For each station, the plots from the left to the right represent the original and corrected radial and transverse components (i), fast and slow waveforms before and after advancing the slow component by the optimal splitting time (ii), particle motion patterns before and after advancing the slow component (iii), and a contour map showing the normalized energy on the corrected transverse component in the XKS time window which is denoted by the two vertical blue bars (iv). The optimal pair of splitting parameters corresponding to the minimum value on the misfit map is indicated by the stars, which are (53.0 ± 1.5°, 1.25 ± 0.07 s) and (−83.0 ± 3.5°, 0.95 ± 0.10 s) for Stations DEHI and PMBT, respectively.

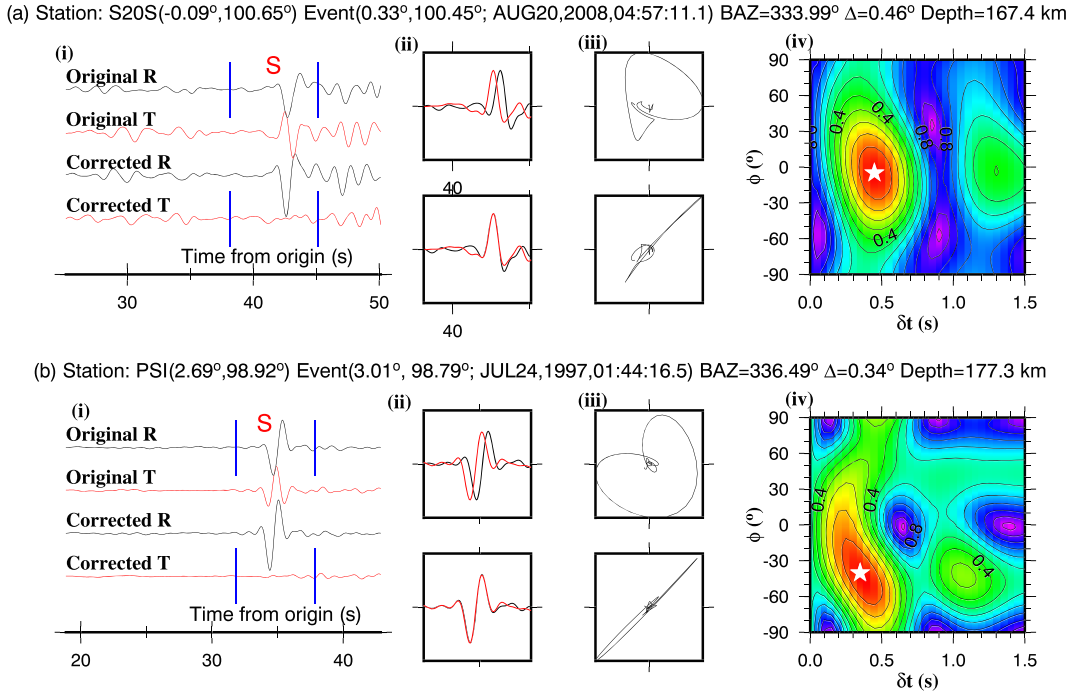

Figure 4. Same as Figure 3 but for local *S* splitting from Stations (a) S20S and (b) PSI. The optimal pairs of splitting parameters are (−5.0 ± 11.0°, 0.45 ± 0.08 s) and (−40.0 ± 4.0°, 0.35 ± 0.05 s) for Stations S20S and PSI, respectively.

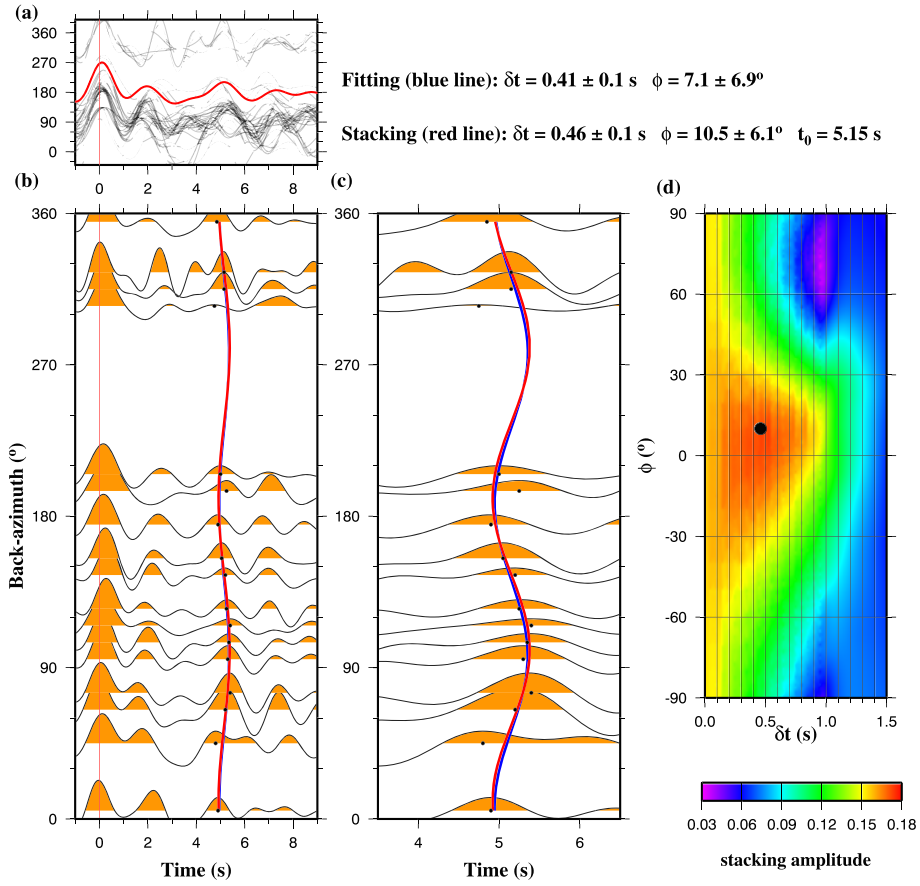

Figure 5. Crustal anisotropy measurement at Station C45B. (a) Original RFs. The red trace represents the result of summation of the individual RFs in time domain. (b). Azimuthal-band-averaged RFs. The black dots show the peak of the *P*-to-*S* conversions from the Moho. The red and blue lines represent the optimal curve calculated based on equation (1) of Kong et al. (2016) using the optimal pair of anisotropy parameters from the stacking and fitting, respectively. (c) Same as (b) but for the time window of 3.5 to 6.5 s. (d) Stacking amplitudes with respect to all the candidate pairs of anisotropy strength and fast orientation. The optimal pair of anisotropy parameters is indicated by the black dot and corresponds to the maximum stacking amplitude.

3.2. Crustal Anisotropy Measurements Using Pms

Averaged azimuthal anisotropy for the whole crust can be obtained by fitting the azimuthal moveout of Pms phases observed on RFs using a sinusoidal function (Kong et al., 2016), and by grid-searching (H. Liu & Niu, 2012; Rumpker et al., 2014; Zheng et al., 2018). Before the computation of the RFs, all the seismograms were band-pass filtered in the frequency band of 0.08 to 0.8 Hz. To improve the accuracy of the picked arrival times of the Pms phase on the RFs, all the RFs were corrected for epicentral distance (Kong et al., 2018). The strength and fast orientation of crustal anisotropy at a given station were obtained by fitting the Pms arrivals using a sinusoidal function. To improve the reliability of the resulting anisotropy parameters, the Pms arrivals were also stacked and the optimal anisotropy parameters were grid-searched using a series of candidate pairs of anisotropy parameters. The optimal pair of fast orientation and strength of crustal anisotropy corresponds to the pair that gives the maximum stacking amplitude (Zheng et al., 2018). For a given station, the crustal anisotropy parameters were calculated by averaging results from the two techniques, if results from the two were comparable (with a difference of 15° or less for the fast orientations and 0.15 s or less for the splitting times); otherwise, results from the station were not used. The uncertainties in the resulting crustal anisotropy measurements are estimated using the standard deviation of the fast orientation and the splitting time (Zheng et al., 2018). Figure 5 shows an example of crustal anisotropy measurement for Station C45B, and more detailed information about the procedure for measuring crustal anisotropy using RFs can be found in Kong et al. (2016) and Zheng et al. (2018).

3.3. Measurement of Upper Mantle Anisotropy

The local *S* splitting in the Sumatra subduction zone is affected by anisotropic structures mainly residing in the crust of the overriding plate and the mantle wedge underneath, and the subcrustal lithospheric mantle is isotropic or weakly anisotropic (Collings et al., 2013). To separate the contributions of the crust and upper mantle to the local *S* splitting, once the crustal and local *S* anisotropy measurements were obtained, splitting parameters associated with upper mantle anisotropy above subducting slab were achieved by applying the layer-stripping method (Rumpker et al., 2014), which is briefly described here. The procedure starts with constructing a set of synthetic RFs containing *P*-to-*S* conversions at an interface (Pds) above which azimuthal anisotropy has a pair of splitting parameters identical to the local *S* splitting. The moveout of the Pds phases relative to the direct *P* was then corrected using the crustal anisotropy measurement for the purpose of removing the crustal contribution from the local *S* splitting (Rumpker et al., 2014). The corrected moveout times were fitted using a sinusoidal function (Kong et al., 2016) to obtain the splitting parameters related to the section of the raypath from the source to the Moho. For the special situation when the fast orientations of the crustal anisotropy and local *S* splitting are parallel with each other, δt of the upper mantle anisotropy can be estimated by subtracting the δt of crustal anisotropy from that of the local *S* splitting. Similarly, when the fast orientations are perpendicular to each other, the splitting time of mantle anisotropy can be estimated by adding the spitting times from local *S* and crustal anisotropy analyses.

4. Results

4.1. Results From XKS Splitting

A total of 169 pairs of well-defined (ranks A or B) XKS splitting parameters, including 9 pairs of PKS, 42 pairs of SKKS, and 118 pairs of SKS measurements (Figure 6a and Table S1), were obtained at 67 individual stations. The splitting times for the whole study area range from 0.4 to 1.8 s with a mean value of 0.9 ± 0.03 s. As shown in Figure 6, when the splitting parameters are plotted based on their location of the ray-piercing points at ~200 km, a systematic lateral variation of the fast orientations can be observed. For XKS measurements with the ray-piercing points located beneath the fore-arc region, the mean δt is 1.17 ± 0.06 s, and the fast orientations are dominantly NE-SW, which is approximately normal to the strike of the Sumatra trench. In contrast, measurements with ray-piercing points located beneath the arc and back-arc regions are characterized by a smaller mean δt of 0.84 ± 0.04 s and mostly trench-parallel fast orientations. We examine the possible existence of complex anisotropy which is mostly characterized by periodic azimuthal variations of the splitting parameters (Silver & Savage, 1994), and find that a vast majority of the stations exhibit azimuthally independent splitting parameters (e.g., Station BKNI shown in Figure 7), suggesting that the observed splitting parameters can be represented by a single anisotropic layer (or multiple layers with the same or orthogonal fast orientations) with a horizontal axis of symmetry. At Station PSI and a few other stations with XKS rays that traversed different tectonic units, the fast orientations are piercing-point dependent (Figure 7). Our XKS splitting results and those in Collings et al. (2013) and Hammond et al. (2010) are generally consistent, but our results provide more spatial coverage (Figures 1 and 6).

4.2. Results From Splitting of Local *S*

In the study, 115 pairs of Quality A or B local *S* splitting parameters with a focal depth range of 26 to 365 km were obtained at 52 stations (Figure 6b and Table S2). The fast orientations of the resulting measurements are dominantly NW-SE with a circular mean of 142.6 ± 30.9° that is in accordance with the strike of the Sumatra trench. The splitting times range from 0.1 to 1.05 s with a mean value of 0.46 ± 0.02 s, and are generally positively correlated with the distance from the station to the trench (Figure 8). The largest δt measurements ranging from 0.3 to 1.04 s are found at Station PSI which is the closest station to the Toba supervolcano among all the stations. The mean δt of local *S* splitting at this station is 0.81 ± 0.04 s, which is significantly higher than that of the rest of the stations (0.35 ± 0.02 s).

4.3. Results From Sinusoidal Moveout of *P*-to-*S* Conversions From the Moho

As shown in Figure 6b, well-defined crustal anisotropy measurements were achieved at seven stations (Table S3), with an average δt value of 0.28 ± 0.05 s. The fast orientations of the resulting crustal anisotropy measurements are dominantly NW-SE with a circular mean of 125.8 ± 43.8°, which are generally consistent with the dominant fast orientation of the local *S* splitting parameters and the strike of the Sumatra trench.

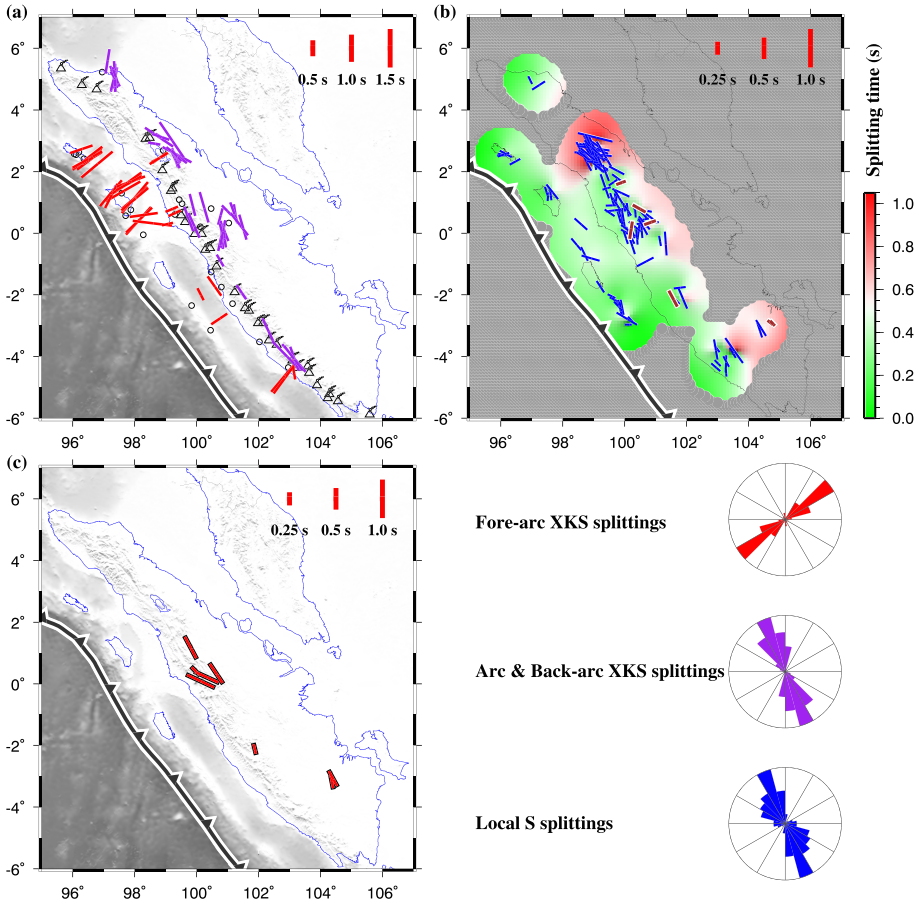

Figure 6. (a) Resulting XKS splitting parameters plotted above the ray-piercing locations at 200-km depth. The red bars show the measurements with the locations in the fore-arc, and the purple bars are those located in the arc and back-arc. The circles are station locations with XKS SWS measurement. (b) The individual (blue bars) well-defined local *S* splitting measurements plotted at the midpoint between the event and station. The background color denotes the splitting time. The brown bars show the distribution of the resulting crustal anisotropy measurements from RFs. (c) Anisotropy measurements of the layer between the Moho and the subducting slab. The rose diagrams from top to bottom represent the fast orientations of XKS splitting in the fore-arc region, XKS in the arc and back-arc, and the local *S* splitting measurements, respectively.

4.4. Quantification of Subcrustal Anisotropy

Totally eight pairs of local *S* splitting parameters were observed (Figure 6c and Table S4) at five stations at which crustal anisotropy measurements were obtained as well. To characterize the upper mantle anisotropy above the subducted slab, we applied the layer-stripping method and obtained eight pairs of anisotropy measurements that have a circular mean Φ of 144.4 ± 20.0° and an average δt value of 0.51 ± 0.08 s. The fast orientations of the observed subcrustal anisotropy are in general agreement with the trench-parallel fast orientations of the *P* wave anisotropy at depth 50 and 150 km obtained by a recent *P* wave anisotropic tomography study (Huang et al., 2015).

5. Discussion

5.1. Mantle Wedge Anisotropy Associated With Trench-Parallel Mantle Flow

The SWS parameters obtained using the local events, which occurred along the subducting slab and thus the resulting anisotropy reflects the combined crustal, lithospheric mantle and mantle wedge anisotropy, are generally consistent with those from previous studies (e.g., Collings et al., 2013; Hammond et al., 2010), and exhibit mostly trench parallel Φ for the whole study area (Figure 6). A major difference between our

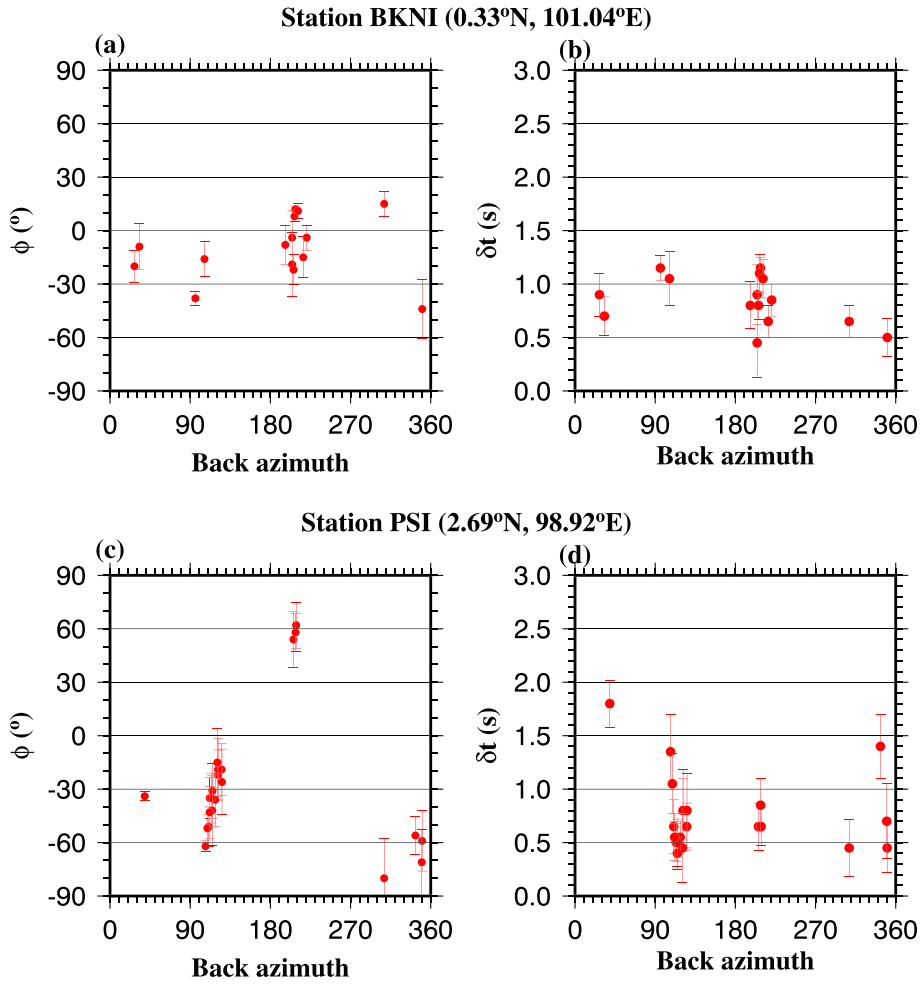

Figure 7. Results of SWS analysis using data recorded by Stations (a and b) BKNI and (c and d) PSI. (a and c) Fast orientations plotted against back azimuth. (b and d) Splitting times plotted against back azimuth.

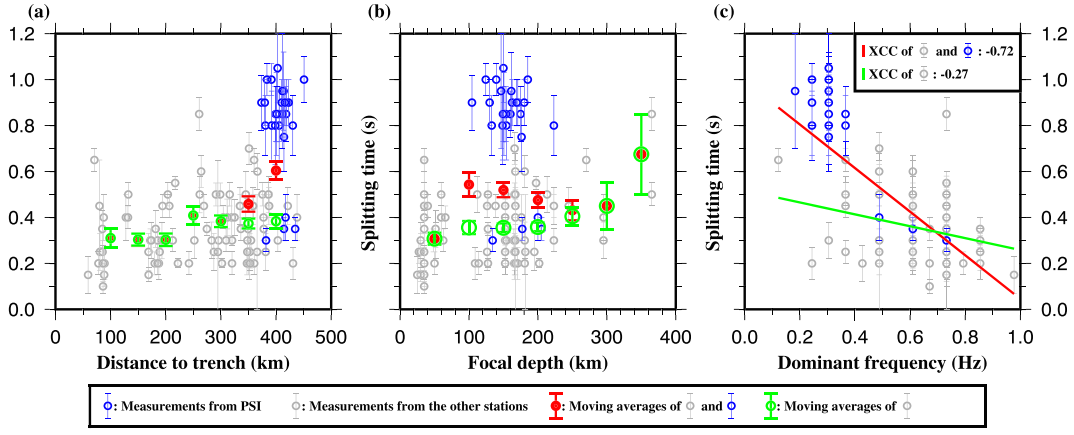

Figure 8. (a) Individual local *S* splitting time from Station PSI (blue circles) and the other stations (gray circles) plotted against the distance from the trench to the midpoint between the events and stations. Red and green circles represent the moving averages with a width of 100 km calculated using all the measurements with and without the ones from PSI, respectively. (b) Same as (a) but plotted with respect to the focal depth. (c) Same as (a) but plotted over the dominant frequency. The red line denotes the best fit using all data, and the green line is the best fit without measurements from PSI. XCC = cross-correlation coefficient.

results and those in Collings et al. (2013) is that the fast orientations observed at the back-arc region are dominantly trench-normal in Collings et al. (2013) while it is mostly trench-parallel in our study (Figure 6).

One of the striking characteristics for the observed local *S* splitting measurements is that there is an apparent positive correlation between the splitting time and the distance from the station to the trench (Figures 6b and 8). However, such a relationship is heavily dependent on the large splitting times observed at Station PSI near the Toba volcano. Probably due to the higher attenuation associated with a high degree of crustal partial melting related to the Toba volcano, the dominant frequency of the local *S* waves observed at PSI is lower than that observed at other stations (Figure 8c). Previous studies indicate that under certain circumstances, larger splitting times are observed for lower frequencies (Long, 2013; Marson-Pidgeon & Savage, 1997). In addition to the LPO of anisotropic minerals in the upper mantle, aligned melting inclusions could also generate seismic anisotropy by shape-preferred orientation (SPO) of the inclusions. The influence of the melting inclusions on the splitting of the local *S* waves depends on the relationship between the spacing of the melting inclusions and the sampling range of the *S* wave (e.g., Greve et al., 2008). Compared to the high-frequency local *S* waves, the low-frequency *S* waves have a longer wavelength and greater Fresnel zones. Thus, the larger splitting times observed at PSI could suggest frequency-dependent anisotropy, and can be attributed to the larger size of sampled melting inclusions beneath the Toba volcano by lower frequency components. When observations from PSI are removed, the splitting times show a general increase with the focal depth (green circles in Figure 8b), a relationship that is more obvious than that between the splitting times and the distance from the trench to the midpoint between the events and stations (green circles in Figure 8a). As discussed below, this difference could indicate that relative to the distance from the trench, the focal depth is a better measure of the length of the raypath in the mantle wedge.

Previous studies reported contrasting conclusions in terms of the origin of the anisotropy characterized by the local *S* splitting. Hammond et al. (2010) suggested that the anisotropy mostly resides in the upper 40 km of the overriding plate, resulted from the SPO of vertically aligned cracks deformed by processes in the overriding Sunda Plate, while Collings et al. (2013) advocated a two-layer anisotropy model above the subducted slab with the upper layer residing in the crust of the overriding plate caused by the SPO of fractures, and the lower layer deformed by the two-dimensional corner flow associated with the slab subduction. The debate in the origin of anisotropy measured by local *S* splitting could be partially addressed by isolating crustal contribution to the observed local *S* splitting (Figure 6c). In this study, we attribute the crustal anisotropy measurements to the SPO of the fractures in the crust (Collings et al., 2013; Hammond et al., 2010), the local *S* splitting observed at most of the stations to the mantle wedge, and the subcrustal lithosphere of the Sunda Plate has insignificant contributions to the observed local *S* wave splitting, for the following reasons:

1. The δt of local *S* splitting measurements correlates positively with the focal depth (Figure 8b), suggesting that δt increases with greater length of raypath in the mantle wedge.
2. Previous studies reported that the crust of the overriding plate in this area is ~30 km thick (Collings et al., 2012) and the thickness for the lithosphere of the overriding plate is less than ~70 km (Steinberger & Becker, 2018), suggesting that the thickness of the lithospheric mantle is less than 40 km. Compared to the underlying mantle wedge that has a thickness up to ~340 km, the contribution of the lithospheric mantle to the local *S* splitting is limited.

If an anisotropy model composed of a single layer with a horizontal axis of symmetry is assumed, the mantle wedge is azimuthally anisotropic with a trench-parallel fast orientation (Figure 9), which is most likely caused by the LPO of olivine (Zhang & Karato, 1995) induced by horizontal mantle wedge flow that is trench-parallel. Such a mantle flow system is caused by the "escaping" of subslab flow from the slab window that is suggested beneath northern Sumatra (Figure 1; Hall & Spakman, 2015; S. Liu et al., 2018). When an entrained flow in subslab mantle is blocked by the mantle transition zone as a slab subducting, the flow is forced to flow horizontally parallel to the trench, and enters mantle wedge in the presence of a slab window (Long & Silver, 2008; Long & Wirth, 2013).

5.2. Subslab Mantle Flow Field

Results of XKS splitting analysis reflect integrated azimuthal anisotropy from the core–mantle boundary, where the XKS phases are generated, to the receiver. For the XKS measurements, the layers that could contribute to the observed anisotropy include the subslab mantle, the subducted slab, and the layer above the

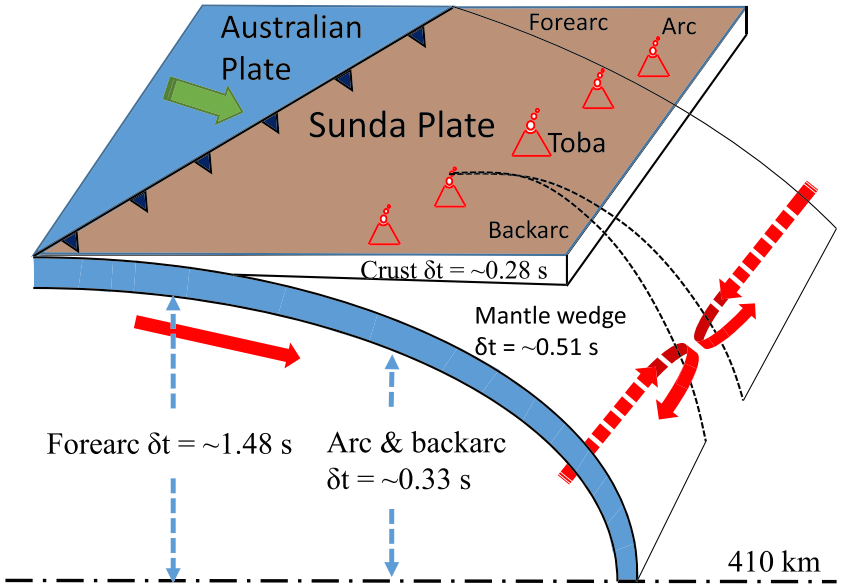

Figure 9. Schematic diagram showing the mantle flow field in the Sumatra subduction zone. The estimated splitting times in the subslab mantle, the mantle wedge, and the crust of the overriding plate are labeled.

subducted slab. The XKS splitting measurements obtained in the study mainly reflect anisotropic structures outside the subducted slab for several reasons.

1. If fossil anisotropy that was formed during the formation of the plate exists in the subducted Australian Plate, the olivine should be N-S oriented due to the north-south plate motion at that time (Hammond et al., 2010; Lithgow-Bertelloni & Richards, 1998), thus resulting in anisotropy with dominantly N-S fast orientations that are inconsistent with the XKS splitting measurements obtained in the study.
2. Previous studies suggested that anisotropy could be induced by the hydration and serpentinization of faults in the subducted plate (Faccenda et al., 2008). In the Sumatra subduction zone, the strike of the faults is N-S trended (Deplus et al., 1998; Graindorge et al., 2008), which orients differently from the XKS splitting parameters either beneath the fore-arc or the arc and back-arc region. Therefore, we infer that the teleseismic XKS splittings are mainly caused by the anisotropic structures outside the subducted slab.

Similarly, the splitting parameters for the subslab anisotropy were obtained by comparing the XKS and local *S* anisotropy measurements. Beneath the fore-arc region, since the fast orientations of the XKS splitting and the local S splitting are nearly orthogonal, the δt of subslab anisotropy is estimated by $\delta t_{XKS} + \overline{\delta t}_{local\ S}$, where the formal represents the δt of the XKS splitting measurements in the fore-arc region, and the latter is the averaged δt of the local *S* splitting measurements from stations in the same region. The resulting δt values have a mean of 1.48 ± 0.06 s. Beneath the arc and back-arc regions, the δt of subslab anisotropy was estimated by subtracting the mean δt of local *S* splitting from that of the XKS splitting, which has a mean value of 0.33 ± 0.04 s.

The resulting subslab anisotropy parameters, when combined with the mantle wedge anisotropy, can be adequately explained by the *A*-, *C*-, or *E*-type LPO of olivine fabric deformed by three-dimensional toroidal flow (Long & Silver, 2008, 2009). Beneath the fore-arc, the subslab mantle flow is entrained with the downgoing Australian Plate, resulting in trench-normally oriented anisotropy. As the entrained mantle flow going deeper, due to the viscosity contrast between the upper mantle and MTZ, the mantle flow is blocked and forced to flow parallel to the trench (Figure 9). Given the presence of a slab window beneath northern Sumatra (Hall & Spakman, 2015; S. Liu et al., 2018), the subslab flow enters the mantle wedge through the slab window, resulting in trench-parallel horizontal mantle flow in the mantle wedge as evidenced by the mostly trench-parallel fast orientations observed from the local *S* splitting. Such a flow system has been suggested to account for the anisotropy detected in the mantle wedge above other subducting slabs, such as those in the Alaskan subduction zone (Venereau et al., 2019) and the subduction of the Pacific slab beneath Japan (Ma et al., 2019).

6. Conclusions

Anisotropic structures in the crust of the overriding plate, the mantle wedge, and the subslab mantle in the Sumatra subduction zone were systematically investigated by applying the shear wave splitting analyses using teleseismic XKS and local *S* phases, as well as systematic azimuthal variations of the *P*-to-*S* conversions from the Moho on teleseismic receiver functions. Comparisons between the XKS splitting parameters, local *S* splitting, and crustal anisotropy measurements suggest that the mantle wedge is azimuthally anisotropic with a dominantly trench-parallel fast orientation, while the fast orientation of the subslab anisotropy is trench-normal beneath the fore-arc and trench-parallel beneath the arc and back-arc. The spatial distribution of the anisotropy measurements constrained using shear waves with different origin depths can be explained by a mantle flow model that is driven by slab subduction and trench migration, and modulated by a slab window.

Acknowledgments
We thank the IRIS DMC (http://ds.iris.edu/ds/) and GEOFON (doi:10.14470/TR560404) for providing the passive seismic data. Constructive reviews from Zhouchuan Huang, an anonymous reviewer, and Editor Maureen Long significantly improved the manuscript. The study was supported by the Scientific Research Fund of the Second Institute of Oceanography SOA (HYGG1802), the Natural Science Foundation of China (41890811, 41976071, 41706044, 41776053), and the U.S. National Science Foundation (1830644 to K.L. and S.G., and 1919789 to S.G.).

References

Ando, M., Ishikawa, Y., & Wada, H. (1980). *S*-wave anisotropy in the upper mantle under a volcanic area in Japan. *Nature*, *286*, 43–46.
Argus, D. F., Gordon, R. G., & DeMets, C. (2011). Geologically current motion of 56 plates relative to the no-net-rotation reference frame. *Geochemistry, Geophysics, Geosystem*, *12*, Q11001. https://doi.org/10.1029/2011GC003751
Ben Ismail, W., & Mainprice, D. (1998). An olivine fabric database: An overview of upper mantle fabrics and seismic anisotropy. *Tectonophysics, 296*, 145-157. https://doi.org/10.1016/S0040-1951(98)00141-3
Candra, A. D., Santosa, B. J., & Rachman, G. (2017). Seismic anisotropy analysis beneath Sumatra revealed by shear-wave splitting. *Indonesian Journal on Geoscience*, *4*, 169–179. https://doi.org/10.17014/ijog.4.3.169-179
Chesner, C. A., & Luhr, J. F. (2010). A melt inclusion study of the Toba Tuffs, Sumatra, Indonesia. *Journal of Volcanology and Geothermal Research*, *197*, 259–278. https://doi.org/10.1016/j.jvolgeores.2010.06.001
Chesner, C. A., Rose, W. I., Deino, A., Drake, R., & Westgate, J. A. (1991). Eruptive history of Earth's largest Quaternary caldera (Toba, Indonesia) clarified. *Geology*, *19*, 200–203. https://doi.org/10.1130/0091-7613 (1991)019<0200:EHOESL>2.3.CO;2
Collings, R., Lange, D., Rietbrock, A., Tilmann, F., Natawidjaja, D., Suwargadi, B., et al. (2012). Structure and seismogenic properties of the Mentawai segment of the Sumatra subduction zone revealed by local earthquake traveltime tomography. *Journal of Geophysical Research*, *117*, B01312. https://doi.org/10.1029/2011JB008469
Collings, R., Rietbrock, A., Lange, D., Tilmann, F., Nippress, S., & Natawidjaja, D. (2013). Seismic anisotropy in the Sumatra subduction zone. *Journal of Geophysical Research*, *118*, 5372–5390. https://doi.org/10.1002/jgrb.50157
Deplus, C., Diament, M., Hebert, H., Bertrand, G., Dominguez, S., Dubois, J., et al. (1998). Direct evidence of active deformation in the eastern Indian oceanic plate. *Geology*, *26*, 131–134. https://doi.org/10.1130/0091-7613(1998)026<0131:DEOADI>2.3.CO;2
Evans, R. (1984). Effects of the free surface on shear wavetrains. *Geophysical Journal International*, *76*, 165–172. https://doi.org/10.1111/j.1365-246X.1984.tb05032.x
Faccenda, M., Burlini, L., Gerya, T. V., & Mainprice, D. (2008). Fault-induced seismic anisotropy by hydration in subducting oceanic plates. *Nature*, *455*, 1097–1100. https://doi.org/10.1038/nature07376
Graindorge, D., Klingelhoefer, F., Sibuet, J.-C., McNeill, L., Henstock, T. J., Dean, S., et al. (2008). Impact of lower plate structure on upper plate deformation at the NW Sumatran convergent margin from seafloor morphology. *Earth and Planetary Science Letters*, *275*, 201–210. https://doi.org/10.1016/j.epsl.2008.04.053
Greve, S. M., Savage, M. K., & Hofmann, S. D. (2008). Strong variations in seismic anisotropy across the Hikurangi subduction zone. *North Island, New Zealand, Tectonophysics*, *462*, 7–21. https://doi.org/10.1016/j.tecto.2007.07.011
Hall, R., & Spakman, W. (2015). Mantle structure and tectonic history of SE Asia. *Tectonophysics*, *658*, 14–45. https://doi.org/10.1016/j.tecto.2015.07.003
Hammond, J. O. S., Wookey, J., Kaneshima, S., Inoue, H., Yamashina, T., & Harjadi, P. (2010). Systematic variation in anisotropy beneath the mantle wedge in the Java-Sumatra subduction system from shear-wave splitting. *Physics of the Earth and Planetary Interiors*, *178*, 189–201. https://doi.org/10.1016/j.pepi.2009.10.003
Huang, Z., Zhao, D., & Wang, L. (2015). P wave tomography and anisotropy beneath Southeast Asia: Insight into mantle dynamics. *Journal of Geophysical Research*, *120*, 5154–5174. https://doi.org/10.1002/2015JB012098
Jung, H., & Karato, S. (2001). Water-induced fabric transitions in olivine. *Science*, *293*(5534), 1460–1463. https://doi.org/10.1126/science.1062235
Karato, S., Jung, H., Katayama, I., & Skemer, P. (2008). Geodynamic significance of seismic anisotropy of the upper mantle: New insights from laboratory studies. *Annual Review of Earth and Planetary Sciences*, *36*, 59–95. https://doi.org/10.1146/annurev.earth.36.031207.124120
Kong, F., Gao, S. S., Liu, K. H., Song, J., Ding, W., Fang, Y., et al. (2018). Receiver function investigations of seismic anisotropy layering beneath Southern California. *Journal of Geophysical Research*, *123*, 10,672–10,683. https://doi.org/10.1029/2018JB015830
Kong, F., Wu, J., Liu, K. H., & Gao, S. S. (2016). Crustal anisotropy and ductile flow beneath the eastern Tibetan Plateau and adjacent areas. *Earth and Planetary Science Letters*, *442*, 72–79. https://doi.org/10.1016/j.epsl.2016.03.003
Koulakov, I., Kasatkina, E., Shapiro, N.M., Jaupart, C., Vasilevsky, A., EI Khrepy, S., Al-Arifi, N., & Smirnov, S. (2016). The feeder system of the Toba supervolcano from the slab to the shallow reservoir. *Nature Communications, 7*, 12228. https://doi.org/10.1038/ncomms12228
Lithgow-Bertelloni, C., & Richards, M. A. (1998). The dynamics of Cenozoic and Mesozoic plate motions. *Reviews of Geophysics*, *36*, 27–78. https://doi.org/10.1029/97RG02282
Liu, H., & Niu, F. (2012). Estimating crustal seismic anisotropy with a joint analysis of radial and transverse receiver function data. *Geophysical Journal International.*, *188*, 144–164. https://doi.org/10.1111/j.1365-246X.2011.05249.x
Liu, K. H., & Gao, S. S. (2010). Spatial variations of crustal characteristics beneath the Hoggar swell, Algeria, revealed by systematic analyses of receiver functions from a single seismic station. *Geochemistry, Geophysics, Geosystem*, *11*, Q08011. https://doi.org/10.1029/2010GC003091

Liu, K. H., & Gao, S. S. (2013). Making reliable shear-wave splitting measurements. *Bulletin of the Seismological Society of America*, *103*, 2680–2693. https://doi.org/10.1785/0120120355

Liu, K. H., Gao, S. S., Gao, Y., & Wu, J. (2008). Shear wave splitting and mantle flow associated with the deflected Pacific slab beneath northeast Asia. *Journal of Geophysical Research*, *113*, B01305. https://doi.org/10.1029/2007JB005178

Liu, S., Suardi, I., Yang, D., Wei, S., & Tong, P. (2018). Teleseismic traveltime tomography of northern Sumatra. *Geophysical Research Letters*, *45*. https://doi.org/10.1029/2018GL078610

Long, M. D. (2013). Constraints on subduction geodynamics from seismic anisotropy. *Reviews of Geophysics*, *51*, 76–112. https://doi.org/10.1002/rog.20008

Long, M. D., & Silver, P. G. (2008). The subduction zone flow field from seismic anisotropy: A global view. *Science*, *319*(5861), 315–318. https://doi.org/10.1126/science.1150809

Long, M. D., & Silver, P. G. (2009). Mantle flow in subduction systems: The subslab flow field and implications for mantle dynamics. *Journal of Geophysical Research*, *114*, B10312. https://doi.org/10.1029/2008JB006200

Long, M. D., & Wirth, E. A. (2013). Mantle flow in subduction systems: The mantle wedge flow field and implications for wedge processes. *Journal of Geophysical Research*, *118*, 583–606. https://doi.org/10.1002/jgrb.50063

Lynner, C., & Long, M. D. (2014). Sub-slab anisotropy beneath the Sumatra and circum-Pacific subduction zones from source-side shear wave splitting observations. *Geochemistry, Geophysics, Geosystems*, *15*, 2262–2281. https://doi.org/10.1002/2014GC005239

Ma, J., Tian, Y., Zhao, D., Liu, C., & Liu, T. (2019). Mantle dynamics of western Pacific and East Asia: New insights from *P* wave anisotropic tomography. *Geochemistry, Geophysics, Geosystems*, *20*. https://doi.org/10.1029/2019GC008373

Marson-Pidgeon, K., & Savage, M. K. (1997). Frequency-dependent anisotropy in Wellington, New Zealand. *Geophysical Research Letters*, *24*, 3297–3300. https://doi.org/10.1029/97GL03274

Rumpker, G., Kaviani, A., & Latifi, K. (2014). *Ps*-splitting analysis for multilayered anisotropic media by azimuthal stacking and layer stripping. *Geophysical Journal International*, *199*, 146–163. https://doi.org/10.1093/gji/ggu154

Silver, P. G., & Chan, W. W. (1991). Shear wave splitting and subcontinental mantle deformation. *Journal of Geophysical Research*, *96*, 16,429–16,454. https://doi.org/10.1029/91JB00899

Silver, P. G., & Savage, M. K. (1994). The interpretation of shear-wave splitting parameters in the presence of two anisotropic layers. *Geophysical Journal International*, *119*, 949–963. https://doi.org/10.1111/j.1365-246x.1994.tb04027.x

Stein, S., & Okal, E. A. (2005). Speed and size of the Sumatra earthquake. *Nature*, *434*, 581–582. https://doi.org/10.1038/434581a

Steinberger, B., & Becker, T. W. (2018). A comparison of lithospheric thickness models. *Tectonophysics*, *746*, 325–338. https://doi.org/10.1016/j.tecto.2016.08.001

Tang, Y., Obayashi, M., Niu, F., Grand, S. P., Chen, Y., Kawakatsu, H., et al. (2014). Changbaishan volcanism in northeast China linked to subduction-induced mantle upwelling. *Nature Geoscience*, *7*, 470–475. https://doi.org/10.1038/NGEO2166

Venereau, C. M. A., Martin-Short, R., Bastow, I. D., Allen, R. M., & Kounoudis, R. (2019). The role of variable slab dip in driving mantle flow at the eastern edge of the Alaskan subduction margin: Insights from shear-wave splitting. *Geochemistry, Geophysics, Geosystems*, *20*, 2018GC008170. https://doi.org/10.1029/2018GC008170

Walpole, J., Wookey, J., Kendall, J., & Masters, T. (2017). Seismic anisotropy and mantle flow below subducting slabs. *Earth and Planetary Science Letters*, *465*, 155–167. https://doi.org/10.1016/j.epsl.2017.02.023

Zhang, S., & Karato, S. (1995). Lattice preferred orientation of olivine aggregates deformed in simple shear. *Nature*, *375*, 774–777. https://doi.org/10.1038/375774a0

Zheng, T., Ding, Z., Ning, J., Chang, L., Wang, X., Kong, F., et al. (2018). Crustal azimuthal anisotropy beneath the southeastern Tibetan Plateau and its geodynamic implications. *Journal of Geophysical Research*, *123*, 9733–9749. https://doi.org/10.1029/2018JB015995